

See discussions, stats, and author profiles for this publication at: <https://www.researchgate.net/publication/40123801>

# Energy-Transfer Dynamics in the LHCII Complex of Higher Plants: Modified Redfield Approach †

ARTICLE *in* THE JOURNAL OF PHYSICAL CHEMISTRY B · JULY 2004

Impact Factor: 3.3 · DOI: 10.1021/jp0496001 · Source: OAI

---

CITATIONS

99

---

READS

66

4 AUTHORS, INCLUDING:



**Herbert Van Amerongen**

Wageningen University

**221** PUBLICATIONS **6,413** CITATIONS

SEE PROFILE



**Rienk van Grondelle**

VU University Amsterdam

**647** PUBLICATIONS **23,687** CITATIONS

SEE PROFILE

# Energy-Transfer Dynamics in the LHCII Complex of Higher Plants: Modified Redfield Approach<sup>†</sup>

Vladimir I. Novoderezhkin,<sup>‡</sup> Miguel A. Palacios,<sup>§</sup> Herbert van Amerongen,<sup>#</sup> and Rienk van Grondelle<sup>\*,§</sup>

A. N. Belozersky Institute of Physico-Chemical Biology, Moscow State University, Leninskie Gory, 119992, Moscow, Russia, Department of Biophysics, Faculty of Sciences, Vrije Universiteit, De Boelelaan 1081, 1081 HV Amsterdam, The Netherlands, and Laboratory of Biophysics, Department of Agrotechnology and Food Sciences, Wageningen University, Dreijenlaan 3, 6703 HA Wageningen, The Netherlands

Received: January 29, 2004; In Final Form: May 11, 2004

We have modeled energy-transfer dynamics in the peripheral plant light-harvesting complex LHCII using both standard Redfield theory and its modification for the case of strong exciton–phonon coupling (Zhang, W. M.; Meier, T.; Chernyak, V.; Mukamel, S. *J. Chem. Phys.* **1998**, *108*, 7763). A quantitative simultaneous fit of the absorption (OD), linear dichroism (LD), steady-state fluorescence (FL) spectra at 7–293 K, and transient absorption (TA) kinetics at 77 and 293 K has been obtained using the experimental exciton–phonon spectral density to model the temperature-dependent line shape. We use configurations of the antenna (i.e., chlorophyll (Chl) *a/b* identities, orientations, and site energies) close to those proposed in our previous study (Novoderezhkin, V.; Salverda, J. M.; van Amerongen, H.; van Grondelle, R. *J. Phys. Chem. B* **2003**, *107*, 1893). These configurations have been further adjusted from the fit with the modified Redfield approach. The new (adjusted) models allow a better quantitative explanation of the spectral shapes. A combination of fast (femtosecond) interband energy transfer and slow (picosecond) intraband equilibration can be better reproduced as well. We paid special attention to unravel the origins of the slow components preliminarily assigned to localized states in the previous work. These “bottleneck” states have been directly visualized in this study via selective femtosecond excitation and probing at different wavelengths. In our modeling, these states are determined by two or three (depending on the model) monomeric Chls *a* or *b* shifted to the spectral region of 655–670 nm between the main absorption peaks of Chl *b* (650 nm) and Chl *a* (675 nm). In all configurations we have found these energy-shifted Chls to be bound at mixed sites (i.e., A<sub>3</sub>, A<sub>6</sub>, A<sub>7</sub>, or B<sub>3</sub>). Experiments and self-consistent modeling using the modified Redfield theory allow us to explore the participation of these states in the overall energy-transfer dynamics. This has led to a more complete and physically adequate model for the energy-transfer dynamics in LHCII.

## Introduction

During the past decade, the study of the energy-transfer dynamics in the peripheral light-harvesting complexes from higher plants has attracted much effort<sup>1</sup> following the discovery of the crystal structure of the major antenna complex LHCII.<sup>2</sup> The LHCII structure was modeled with 3.4 Å resolution, which did not allow for a distinction between chlorophyll (Chl) *a* and *b* or between the X- and Y-axes of the Chls. Thus, the identities of the Chls at the 12 discernible binding sites and the direction of their dipole moments were assigned in a hypothetical fashion.

Several site-directed mutagenesis studies of the chlorophyll binding residues have been carried out to determine the Chl identities in LHCII<sup>3–6</sup> and in the similar complex CP29.<sup>7,8</sup> Remelli et al.<sup>3</sup> concluded that the sites A<sub>1</sub>, A<sub>2</sub>, A<sub>4</sub>, A<sub>5</sub>, and B<sub>1</sub> are occupied by Chls *a* and the sites B<sub>2</sub>, B<sub>5</sub>, and B<sub>6</sub> by Chls *b*, whereas A<sub>3</sub>, A<sub>6</sub>, A<sub>7</sub>, and B<sub>3</sub> are “mixed” sites which can bind both Chls *a* and Chls *b*. This result was contested by Rogl and co-workers<sup>4,6</sup> who assumed that mixed binding sites cannot occur in native complexes and concluded that the A<sub>3</sub> and B<sub>3</sub>

sites both bind Chl *a*. In a more recent assignment of Bassi [private communication] a Chl *b* is proposed to bind at site A<sub>7</sub>, whereas the other three sites remain mixed. Using the identities proposed by Remelli et al., Işeri and Gülen<sup>9</sup> attempted to assign the orientations of the Chls by modeling the absorption (optical density, OD) and linear dichroism (LD) spectra of LHCII using an exciton model without spectral disorder. They supposed that all mixed sites have an equal probability to bind Chl *a* or *b*, thus considering all 16 possible configurations of A<sub>3</sub>A<sub>6</sub>A<sub>7</sub>B<sub>3</sub> from *aaaa* to *bbbb*. A satisfactory fit of the OD and LD spectra was obtained for the orientations A<sub>1</sub>A<sub>2</sub>A<sub>3</sub>A<sub>4</sub>A<sub>5</sub>A<sub>6</sub>A<sub>7</sub>B<sub>1</sub>B<sub>2</sub>B<sub>3</sub>B<sub>5</sub>B<sub>6</sub> = 0100000 00110, with the notation 0 meaning orientation of the Q<sub>y</sub> transition dipole along the N<sub>A</sub>–N<sub>C</sub> axis and 1 along N<sub>B</sub>–N<sub>D</sub> axis, as proposed by Gülen et al.<sup>10</sup> A satisfactory exciton model in the context of the Redfield theory, accounting for spectral disorder and weak exciton–phonon coupling, has recently been developed.<sup>11</sup> Good fits of the OD and LD spectra were found for the A<sub>3</sub>A<sub>6</sub>A<sub>7</sub>B<sub>3</sub> = *abab*, *baab*, and *baba* configurations and 0000000 00100 orientations and for the *bbba* configuration with orientations 0100000 00110 of the transition dipole moments.<sup>11</sup> An exciton theory capable of explaining the phonon-induced temperature dependence of the OD spectrum was developed by Renger and May.<sup>12</sup> They concluded that the OD spectra at 40, 80, and 120 K can be quantitatively reproduced using the model with Kühlbrandt’s original assign-

<sup>†</sup> Part of the special issue “Gerald Small Festschrift”.

<sup>\*</sup> To whom correspondence should be addressed. E-mail: rienk@nat.vu.nl. Fax: +31-20-4447899.

<sup>‡</sup> Moscow State University.

<sup>§</sup> Vrije Universiteit.

<sup>#</sup> Wageningen University.

ment<sup>2</sup> (the sites A<sub>1–7</sub> are occupied by Chls *a* and the sites B<sub>1–3,5,6</sub> by Chls *b*) as well as the modified Kühlbrandt model (in which A<sub>6</sub> changes its identity with B<sub>5</sub>). Modeling of the 77 K circular dichroism (CD) spectrum showed that the original Kühlbrandt model fails to explain the data, whereas the modified model allows a qualitative agreement.

The dynamical behavior of LHCII, specifically the energy transfer between the chlorophylls, was studied with various time-resolved nonlinear spectroscopic methods. Transient absorption (TA) and time-resolved fluorescence studies revealed that Chl *b* to Chl *a* transfer takes place with two major time constants of  $\sim 300$  and  $\sim 600$  fs at 77 K,<sup>13–17</sup> or  $\sim 150$  and  $\sim 600$  fs at room temperature,<sup>13,18–20</sup> and a minor 4–9 ps component. Equilibration within the Chl *a* manifold occurs to a large extent within a few hundred femtoseconds, but upon blue side excitation slow picosecond components are also observed.<sup>14,16</sup> Three-pulse photon echo peak shift (3PEPS) and transient grating (TG) measurements on LHCII at room temperature have been performed recently using 650 and 670 nm excitation, corresponding to the Chl *b* and *a* regions, respectively.<sup>21,22</sup> Whereas the pump–probe technique mainly monitors downhill (“interband”) energy transfer, the three-pulse photon echo technique is more sensitive to the intraband Chl *a*–Chl *a* and Chl *b*–Chl *b* transfer processes.<sup>23</sup> Agarwal et al.<sup>21</sup> analyzed their data using a theory that includes a simple energy-transfer model,<sup>23</sup> based on hopping of localized excitations with phenomenological rate constants as free parameters. They also incorporated exciton–phonon coupling by convoluting the energy-transfer function with a single-site correlation function, which consists of a sum of Gaussian, exponential, and damped cosine contributions. Their modeling showed subpicosecond Chl *b*  $\rightarrow$  Chl *b* transfer for the first time. They also identified contributions from the well-known Chl *b*  $\rightarrow$  Chl *a* transfer processes, which take place with time constants of 150 fs, 600 fs, and 4 ps, and from Chl *a*–Chl *a* equilibration occurring with time constants from 300 fs to 6 ps.

The 3PEPS and TG data of Salverda et al.<sup>22</sup> was analyzed in our recent paper<sup>11</sup> using the Redfield relaxation theory in the basis of the exciton eigenstates. We found a few configurations of the antenna (with specific chlorophyll (Chl) *a/b* identities, orientations, and site energies) which allowed us to quantitatively explain the OD and LD spectra, the superradiance (SR) values, and the TA, TG, and 3PEPS kinetics at different excitation wavelengths. In our model the Chl *b* absorption region reflects localized monomer states and partially delocalized dimer states giving rise to an averaged delocalization length of individual exciton levels of 1.1–1.6. The individual exciton states in the Chl *a* region can be delocalized over 2–2.5 molecules. Due to the nonparallel orientation of the monomeric dipoles, the dipole strength enhancement of an individual exciton state is smaller than the delocalization length. Thus we found a dipole strength of 1.5–2 (in units of monomeric dipole strength) for the second exciton level ( $k = 2$ ) in the Chl *a* band. This is in agreement with the nonlinear absorption and nonlinear polarization data suggesting the existence of one spectral form with a dipole strength of 2.3.<sup>24</sup> Mixing of this superradiant state with the weaker lowest exciton states results in an SR value of 1–1.2 in agreement with the experimental data.<sup>25</sup> We found that at room temperature the intraband (Chl *b*  $\rightarrow$  Chl *b* and Chl *a*  $\rightarrow$  Chl *a*) energy-transfer dynamics includes subpicosecond (250–600 fs) exciton relaxation within dimeric or, in the Chl *a* band, more complicated clusters, subpicosecond (600–800 fs) hopping between spatially separated clusters (in the *a* band), and “slow” (picosecond) migration between localized states. The interband

(Chl *b*  $\rightarrow$  Chl *a*) transfer is characterized by the presence of very fast channels, the fastest taking only 120 fs, which connect both localized and dimeric *b* states with the *a* band.<sup>11</sup>

For some configurations of the monomeric LHCII subunit (*bbaa*, *baba*) either the highest state in the Chl *a* region,  $k = 7$ , or the state  $k = 6$ , is almost completely localized on the most blue-shifted Chl *a* molecule. These localized states give rise to a relatively long-lived kinetic component, in agreement with earlier pump–probe studies.<sup>14,16</sup> For other configurations (*baab*, *abab*) the blue side of the Chl *a* absorption band is determined by higher exciton levels of strongly coupled clusters producing rather fast downhill transfer in the Chl *a* band. These configurations allowed us to explain the TG and 3PEPS kinetics upon broadband 650 or 670 nm excitation as well as TA kinetics probed at two wavelengths (i.e., 650 and 680 nm).<sup>11</sup> However, it is evident that such configurations cannot explain the kinetics near 660–670 nm with a pronounced contribution of long-lived kinetic components.

In this paper we model the two-color TA kinetics measured at probe wavelengths from 641 to 689 nm with a step of 3 nm upon 650 nm excitation, thus allowing one to visualize the evolution of the whole spectrum reflecting an interplay of the intra- and interband transfers in LHCII. The OD, LD, and steady-state nonselective fluorescence (FL) spectra measured at temperatures from 7 to 293 K provided us with information about exciton–phonon coupling. To model the data we use the standard Redfield theory<sup>26,27</sup> as well as its modified version generalized to the case of strong exciton–phonon coupling.<sup>28</sup>

Recently Yang and Fleming<sup>36</sup> compared the energy-transfer rates within a simplest exciton system (molecular dimer) calculated with the Förster, Redfield, and modified Redfield theories. Numerical comparison of the three models (using the same phonon spectral density) shows that in the case of relatively weakly coupled pigments (20 cm<sup>−1</sup> coupling strength) with a small (0–100 cm<sup>−1</sup>) energy gap, the Redfield rates can be up to 10–100 times larger than the Förster rates. This situation roughly corresponds to the intraband Chl *b*  $\rightarrow$  Chl *b* transfers involving monomeric states. On the other hand, for a larger energy gap between monomers (200–1000 cm<sup>−1</sup>), the Redfield equation always gives significantly slower rates than the Förster equation (for any value of the intermolecular coupling). This range corresponds to the interband Chl *b*  $\rightarrow$  Chl *a* transfer. In the case of a small gap, the modified Redfield method predicts the same rates as the Redfield rates (both different from the Förster rates in this case), whereas the modified Redfield rates coincide with the Förster rates at large gaps, when the Redfield rates are too slow. It was concluded that the standard Redfield theory only works well for a small energy gap between the interacting states. In this case, the validity of the theory is guaranteed not by a weak coupling to the bath, but by a wide spectrum of phonons. On the other hand, a large energy gap corresponds to the Förster regime. Both these limits are covered by the modified Redfield approach.

In the present study we compare the standard Redfield and modified Redfield approaches in the case of a real antenna system (LHCII complex) using the experimental exciton–phonon spectral density taken from fluorescence line-narrowing (FLN) data for this antenna complex.<sup>29</sup> We found that the modified Redfield theory better reproduces fine features of multicomponent kinetics, including contributions from slow intraband and fast interband transfers.

The experiments shown here provide evidence of long-lived states in the spectral region near 665–671 nm, in agreement with earlier observations<sup>14,16</sup> and consistent with our previous

attempt to model these experiments.<sup>11</sup> A self-consistent fit using the modified Redfield theory allows us to assign these states and to explore their participation in the overall energy-transfer dynamics. This has led to a more detailed and complete model of LHCII.

## Materials and Methods

Trimeric LHCII was purified from spinach<sup>30</sup> using anion-exchange chromatography and the detergent *n*-dodecyl- $\beta$ -D-maltoside (Sigma) for solubilization of the complexes. The samples were diluted in a medium containing 20 mM Hepes buffer at pH 7.8 and 0.03% (w/v) *n*-dodecyl- $\beta$ -D-maltoside. Additionally, 63% (v/v) of glycerol was added for the low-temperature measurements. Measurements were performed at RT using a flow cell (1 mm path length) to avoid photodegradation and at 77 K (Oxford cryostat, DN1704) in a cell which consisted of two acrylic windows glued together with double-sided sticky tape, resulting in a cell with an optical path length of  $\sim 200 \mu\text{m}$ . The ODs of the samples were 0.45 (RT) and 0.66 (77 K) at the Chl *a*  $Q_y$  maximum. Changes in the absorption spectrum during pump-probe measurements due to photodegradation or bleaching of the chromophores are estimated to be at most 2% at RT and less than 1% at 77 K.

Femtosecond laser pulses were obtained from a titanium:sapphire laser oscillator-regenerative amplifier combination (Coherent MIRA seed and RegA 9058) operating at a repetition rate of 125 kHz, which provided 60 fs, 30 nm wide (fwhm) pulses at 800 nm. The output was split into two beams: one of the beams was focused into a sapphire plate to generate a white light continuum used as the probe pulse, and the other beam was used to pump an infrared optical parametric amplifier (OPA 9850, Coherent). The output of the OPA was tuned to  $1.30 \mu\text{m}$  and was frequency doubled to 650 nm. Remaining infrared light was removed with a cutoff filter. The resulting pulse had a bandwidth (fwhm) of  $\sim 19 \text{ nm}$  and a duration of  $\sim 40 \text{ fs}$ . The instrument response function of the setup, estimated from the fwhm of the signal measured after mixing of the pump and probe beams in a BBO crystal at the place of the sample, was  $\sim 70 \text{ fs}$ . In all measurements, the polarization of the pump laser beam was set at the magic angle ( $54.7^\circ$ ) with respect to the probe beam by means of a Berek polarization compensator (New Focus, 5540). Individual transient absorption traces were recorded by lock-in detection (EG&G Model 5210) with the pump beam chopped at frequency  $f = 612 \text{ Hz}$ . The detection wavelength was selected by focusing the white light probe beam into a monochromator.

The beam diameter was  $\sim 160 \mu\text{m}$  in the focus, determined as the fwhm of a Gaussian intensity profile. The excitation intensity used was 0.64 nJ/pulse. Under our experimental conditions, we estimate that, at most, one out of 170 Chl *b* molecules is excited per pulse. Therefore, any annihilation effects can safely be neglected in the results presented in this work.

The FL spectra were taken from ref 25. The OD/LD data was taken from ref 31.

## The Model

We consider a monomeric LHCII complex consisting of 12 chlorophyll (Chl) molecules at sites  $A_1$ ,  $A_2$ ,  $A_3$ ,  $A_4$ ,  $A_5$ ,  $A_6$ ,  $A_7$ ,  $B_1$ ,  $B_2$ ,  $B_3$ ,  $B_5$ , and  $B_6$  (nomenclature from Kühlbrandt et al.<sup>2</sup>), where sites  $A_1$ ,  $A_2$ ,  $A_4$ ,  $A_5$ , and  $B_1$  bind Chls *a*, sites  $B_2$ ,  $B_5$ , and  $B_6$  bind Chls *b*, sites  $A_3$  and  $B_3$  bind each on average 0.5 Chl *a* and 0.5 Chl *b*, and sites  $A_6$  and  $A_7$  together bind 0.5 Chl *a* and 1.5 Chl *b* (based on Remelli et al., ref 3). This means that one LHCII subunit contains on average 6.5 Chls *a* and 5.5 Chls *b*. We checked out all possible realizations of pigment

identities at mixed sites with 7 Chls *a* and 5 Chls *b* per subunit (combinations  $A_3A_6A_7B_3 = abab, abba, baab, baba, aabb, \text{ and } bbaa$ ), as well as the realizations with 6 Chls *a* and 6 Chls *b* per subunit which have 2 Chls *b* on  $A_6$ – $A_7$  (combinations  $A_3A_6A_7B_3 = abbb, bbba$ ). For each of these eight configurations, we tried to obtain a simultaneous fit of the OD, LD, FL, and TA data using different orientations and site energies of the chlorophylls. Calculations have been performed using the expressions given in Appendixes A–D.

The exciton Hamiltonian and the static disorder (site inhomogeneity) model are the same as in our previous study.<sup>11</sup> Instead of weak exciton–phonon coupling with a phenomenological spectral density used previously,<sup>11</sup> here we include strong coupling to phonons/vibrations with the experimental spectral density obtained from FLN data for LHCII.<sup>29</sup> The corresponding line shapes (given in Appendix D) have pronounced vibrational structure and also include a reorganization energy shift (i.e., spectral shift due to reorganization energy associated with the strong coupling of electronic transitions with phonons). As a result the peak position of the exciton components in the OD are significantly different from the eigenvalues  $\omega_k - \omega_g$  obtained from the exciton Hamiltonian. The reorganization energy shift is different for different exciton states (eq D3) so that the site energies obtained in this modeling are nonuniformly blue-shifted as compared with those from ref 11.

The TA kinetics were calculated using the doorway–window representation (Appendix A). The time evolution of the doorway amplitude reflecting one-exciton dynamics is given by the Redfield relaxation tensor. We use both standard Redfield (Appendix B) and modified Redfield (Appendix C) theories in order to compare these two approaches. In the case of standard Redfield theory we can use the full third-order density matrix equation<sup>32,33</sup> instead of the doorway–window representation. In this case we can reproduce a rise of TA at negative delays (in the doorway–window picture we start from zero delay with the initial one-exciton populations integrated over the pump pulse). A more correct result can be obtained if we use the same approach (i.e., density matrix equation) but with the modified Redfield tensor for the second-order population dynamics. This method gives more realistic relaxation rates, but the line shapes are still simple Lorentzians. In the case of broad-band excitation the thus-calculated kinetics are almost the same as in the full-cumulant-expansion method (i.e., using eqs A1–A4, A6, and C1–C3). In the latter case (eqs A3, A4, A6, C1–C3) we get realistic line shapes and relaxation rates, but the kinetics can only be obtained for positive delays.

To calculate the line shapes and relaxation rates we have to specify the spectral density  $C(\omega)$ . In this paper we model the linear and nonlinear spectra obtained with nonselective excitation (and probe). Our criterion for the spectral density choice is the possibility to reproduce nonselective FL profiles at different temperatures (including the low-temperature FL revealing a fine structure of the vibrational wing). Such a spectral density profile can be constructed by direct fitting of the FL spectra with some model profile, for example in the form of eq D2. In principle, the FLN or hole-burning (HB) data is not needed for such a fitting. Alternatively, one can use eq D2 with realistic values of the vibrational frequencies and relative Huang–Rhys factors taken from FLN or HB. At the moment the FLN data for LHCII<sup>29</sup> and HB for PSI<sup>34</sup> are available. The absolute values of the Huang–Rhys factors for Chl *a* obtained in these two studies are significantly different. The reason for such a discrepancy is not clear. The HB data gave much bigger Huang–Rhys factors, which are in better correspondence with



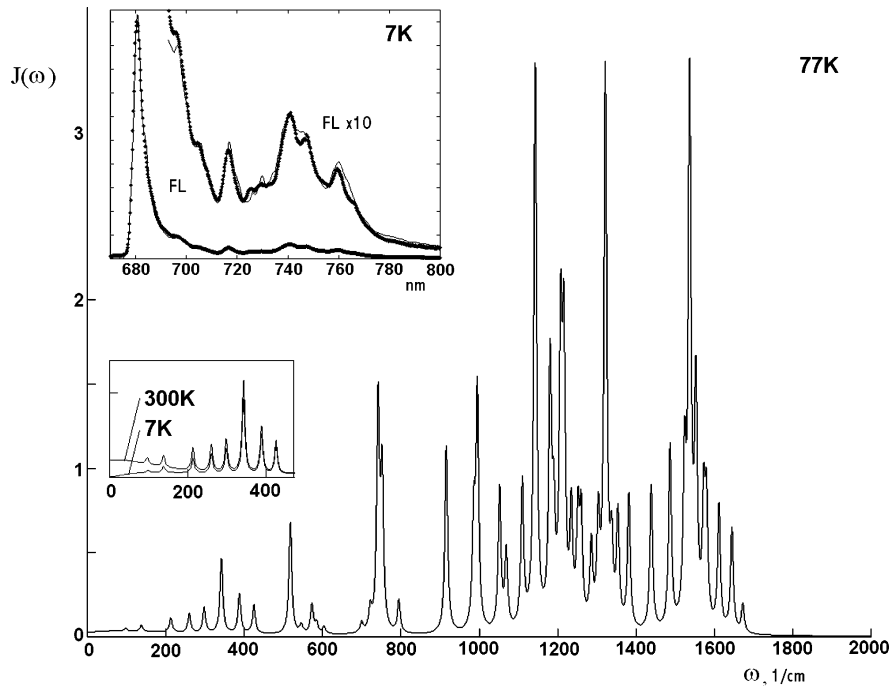


**Figure 1.**  $J(\omega)$  function calculated at 77 K with the parameters determined from the fit of the low-temperature nonselective 7 K fluorescence spectrum of the LHCII complex. To fit the fluorescence profile (see inset in the top) we use the model spectral density  $C(\omega)$  as a sum of an overdamped Brownian oscillator and 48 high-frequency modes with Huang–Rhys factors taken from the FLN experiment.<sup>29</sup> Notice that the low-frequency wing of the  $J(\omega)$  function is temperature-dependent (see inset).

**TABLE 1: Frequencies  $\omega_j$ ,  $\text{cm}^{-1}$ , and Huang–Rhys Factors  $S_j$  for Nuclear Modes  $J = 1\text{--}48$  ( $\sum S_j = 0.7$ )**

$\omega_j$	$S_j$	$\omega_j$	$S_j$	$\omega_j$	$S_j$	$\omega_j$	$S_j$
97	0.023 96	604	0.001 94	1143	0.040 94	1354	0.005 76
138	0.028 81	700	0.001 97	1181	0.017 59	1382	0.006 67
213	0.030 02	722	0.003 94	1190	0.006 67	1439	0.006 67
260	0.026 69	742	0.039 42	1208	0.018 50	1487	0.007 88
298	0.026 69	752	0.025 78	1216	0.017 59	1524	0.006 36
342	0.060 35	795	0.004 85	1235	0.006 97	1537	0.021 83
388	0.024 87	916	0.021 23	1252	0.006 36	1553	0.009 09
425	0.014 86	986	0.010 31	1260	0.006 36	1573	0.004 54
518	0.039 42	995	0.022 74	1286	0.004 54	1580	0.004 54
546	0.002 69	1052	0.012 13	1304	0.005 76	1612	0.004 54
573	0.008 49	1069	0.006 36	1322	0.030 32	1645	0.003 63
585	0.003 03	1110	0.011 22	1338	0.003 94	1673	0.000 97

nonselective FL shapes. On the other hand, the relative Huang–Rhys factors obtained from FLN<sup>29</sup> appear to be reliable.<sup>34</sup> In our modeling of LHCII antenna we use the relative Huang–Rhys factors from FLN (i.e., obtained for the same complex) with their further scaling from the fit of the nonselective fluorescence.

Our model spectral density  $C(\omega)$  (eq D2) includes an overdamped Brownian oscillator with the parameters  $\lambda_0$ ,  $\gamma_0$  and 48 high-frequency modes with frequencies  $\omega_j$ , couplings  $\lambda_j = S_j \omega_j$  (where  $S_j$  is the Huang–Rhys factor of  $j$ th mode), and damping constants  $\gamma_j$  (which are taken to be small, i.e.,  $\gamma_j = 3 \text{ cm}^{-1}$ ). These parameters were taken from the FLN data.<sup>29</sup> The fit of the 7 K FL (determined by the effective spectral density  $C(\omega)/\omega^2$ ) is shown in Figure 1 together with the temperature-dependent  $J(\omega)$  function which determines the relaxation rates between the eigenstates (defined by eq B6, i.e.,  $J(\omega) = J_{ab}(\omega_{ab})$ ). The frequencies,  $\omega_j$ , and  $S_j$  factors adjusted and scaled from the fit are listed in Table 1. Notice that the high-frequency part of the spectral density up to 1000–1200  $\text{cm}^{-1}$  is needed to explain the interband Chl  $b \rightarrow$  Chl  $a$  transfer. In order to obtain quantitatively correct results we use the full spectral density in the range of 0–1700  $\text{cm}^{-1}$ .

Notice that from the fit of the FL, FLN, and HB spectra one can determine only the effective coupling constants in the exciton representation, which are equal to the site-representation values  $\lambda_0$  and  $\lambda_j$  (or  $S_j$ ) multiplied by a participation ratio (eq D3). The latter is different for configurations with a different amount of delocalization of the exciton states. This means that we will need different site-representation couplings in order to reproduce the experimental results using different antenna models. In our modeling we keep the relative  $S_j$  values unchanged (listed in Table 1), but the total Huang–Rhys factor for the high-frequency wing, i.e.,  $S = \sum_j S_j$ , as well as the parameters of the low-frequency Brownian oscillator  $\lambda_0$ ,  $\gamma_0$ , are slightly different for different models of the antenna. The Huang–Rhys factor for the low-frequency part equals 0.6–1.0 in the site representation, where bigger values correspond to models with bigger participation ratio (so that the effective Huang–Rhys factors in the exciton representation lie within a more narrow range of about 0.5–0.65 in agreement with the earlier observed value of 0.6<sup>29</sup>).

We do not consider a possible site-to-site variation of the coupling strength (given by the dimensionless factors  $v_n$  and  $w_n$ ) supposing  $v = 1$  for Chls  $a$  and  $v = v_b$  for Chls  $b$ . Similarly, we suppose that the site inhomogeneity value is  $\sigma$  for Chls  $a$  and  $s_b \sigma$  for Chls  $b$ . Thus we get three adjustable parameters of dynamic disorder, i.e.,  $\lambda_0$ ,  $\gamma_0$ , and  $S$ , one parameter of the static disorder  $\sigma$ , and two parameters of the  $b \rightarrow a$  inhomogeneity, i.e.,  $v_b$ , and  $s_b$ . The effective dipole strength for Chl  $a$  was varied in the 14–18 D<sup>2</sup> range.<sup>1,35</sup>

It is important that our expressions for linear spectra (eq D1) include a relaxation-induced broadening of the exciton states given by their inverse lifetimes, i.e.,  $R_{kkk}$  as suggested in refs 38 and 46. This term was not included in the original theory of Zhang et al.<sup>28</sup> This shortcoming of the theory was first recognized by Ohta et al.<sup>46</sup> In our modeling we tried both versions of the modified Redfield theory, i.e., with and without the relaxation term. When eqs D1 were used without this term

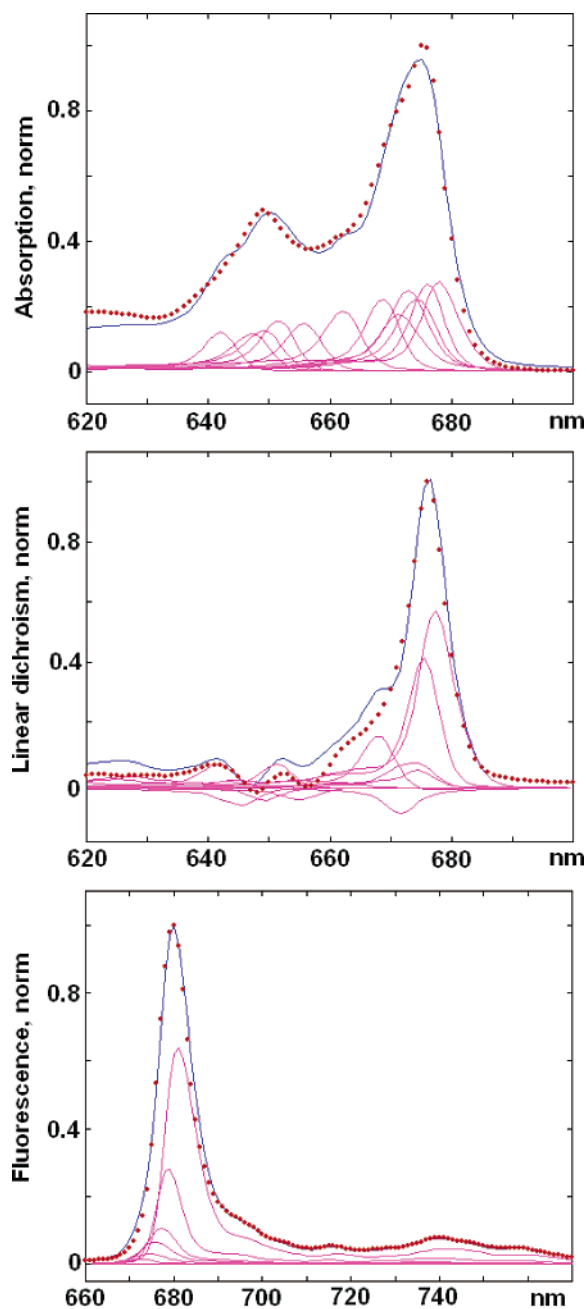


**Figure 2.** Experimental OD, LD, and FL spectra of LHCII at 77 K (points) and the calculated ones (solid blue). Calculated spectra are shown together with individual exciton components (solid pink). Parameters of the model are shown in Table 2 (the first *bbaa* model).

it was difficult to reproduce quantitatively a narrow feature in the OD/LD near 675 nm together with the broader bands at the blue side of the spectra (640–660 nm). Including a relaxation term into eqs D1 allowed us to get better fit (see Figure 2).

## Results

We checked out all possible  $A_3A_6A_7B_3$  configurations trying to reproduce the OD/LD/FL spectra and TA kinetics. Recall that in our previous study we found four configurations with satisfactory OD/LD fits, and two of them (*bbaa*, *baba*) were found to be in agreement with the energy-transfer data (3PEPS, TG, TA).<sup>11</sup> In this paper we have checked more combinations of identities, orientations, and site energies. We found that more or less reasonable OD/LD/FL fits can be obtained for all eight configurations. Only four of them survive after including the TA data into the fit, i.e., the *bbaa*, *baba*, *abba*, and *aabb*

configurations. The parameters of these four models are listed in Table 2. For each model it was possible to find several suitable combinations of the orientations and site energies (see Table 2). Optimization of the site energies was performed using a simple evolutionary algorithm, with a final fine-tuning “by hand”. The best fit was obtained for the *bbaa* configuration. The corresponding OD/LD/FL fit (for 77 K) is shown in Figure 2. Due to more realistic line shapes this fit is much better than the one obtained previously.<sup>9,11</sup> Unfortunately, the LD spectrum is only available for 77 K, but other linear spectra, i.e., the OD and FL spectra, can be satisfactorily reproduced for all temperatures from 7 to 293 K (data not shown).

Notice that the site energies given in Table 2 do not include the reorganization energy shift due to strong coupling to phonons and vibrational modes (this shift is explicitly taken into account by introducing the  $\lambda$  matrices—see Appendixes C and D). Diagonalization of the Hamiltonian containing the thus-determined site energies gives us the energies corresponding to the first moment of the absorption of the  $k$ th exciton state  $\omega_k$ . Due to the presence of high-frequency vibrational satellites this first moment  $\omega_k$  is significantly blue-shifted with respect to the absorption peak of the  $k$ th exciton component (determined by the low-frequency phonon wing of the zero-phonon line). The difference between  $\omega_k$  and the zero-phonon line is given by  $\lambda_{kkkk}$  (eq D3) which is proportional to the exciton–phonon coupling  $\lambda$  and participation ratio of the  $k$ th exciton state. Thus, the actual position of the absorption maximum of the  $k$ th exciton component is red-shifted with respect to the purely electronic transition. The value of this shift is different for different states being determined by the disorder-induced localization length of the  $k$ th exciton state. Such a shift was not present in our previous modeling performed in the limit of weak exciton–phonon coupling.<sup>11</sup>

Chls *a* and Chls *b* contribute to the exciton states peaking around 675 and 650 nm, respectively. The blue-shifted Chls *a* together with red-shifted Chls *b* are responsible for the intermediate states in the 655–665 nm region (Figure 2). For all the models the  $B_1(a)$  pigment is always shifted to the blue (Table 2). This  $B_1$  pigment is strongly coupled to other Chls *a* (mostly to the  $A_1$  and  $A_2$  pigments which contribute to the lowest exciton states) producing a fast relaxation channel from the intermediate 655–665 nm region to the lowest exciton states at the red side of the Chl *a* region. To reproduce the slow decay component of the intermediate states (suggested earlier<sup>14,16</sup>) some monomeric states (localized at one Chl *a* or Chl *b* molecule) should be present in the 655–665 nm region. In our models they can be blue-shifted  $A_3(a)$ ,  $A_6(a)$ ,  $A_7(a)$ , or  $B_3(a)$  and red-shifted  $A_3(b)$ ,  $A_6(b)$ ,  $A_7(b)$ ,  $B_3(b)$ , or  $B_2(b)$  (Table 2).

It is interesting to note that the intermediate localized states are always determined by one, two, or three pigments of the mixed sites  $A_3$ ,  $A_6$ ,  $A_7$ , or  $B_3$ . This implies that changing the pigment identity in our simulations at mixed sites very often gives only minor changes in the overall exciton structure of the complex. These changes do not influence the strongly coupled clusters in the *a* region and dimers in the *b* region, giving just some rearrangement of the localized states. For example, in the *abba* model we got blue-shifted  $A_3(a)$  and red-shifted  $A_7(b)$  (see the first *abba* configuration in Table 2). If  $A_3(a)$  and  $A_7(b)$  turn out to be  $A_3(b)$  and  $A_7(a)$ , respectively, we will switch to the *bbaa* model. But in this case we find that  $A_3(b)$  is red-shifted and  $A_7(a)$  is blue-shifted (see the first *bbaa* configuration in Table 2). It looks like an interchange between the site energies of the  $A_3$  and  $A_7$  pigments both lying in the intermediate region (red-most Chl *b* turns to blue-most Chl *a* and vice versa), or in

**TABLE 2: Parameters of the  $[A_1A_2A_3A_4A_5A_6A_7 B_1B_2B_3B_5B_6]$  Sites for Different  $A_3A_6A_7B_3$  Configurations: Orientations  $N_{B-D}$  in Gülen's Notation,<sup>10</sup> Site Energies  $E$  (Counted from 15 000  $\text{cm}^{-1}$ ), Parameters of the Dynamic Disorder  $\lambda_0$ ,  $\gamma_0$ ,  $S$ ,  $\nu_b$ , Static Disorder,  $\sigma$  and  $s_b$ , and the Effective Dipole Strength  $D^2$  for Chl *a* (in debye)<sup>2a</sup>**


---

$A_3A_6A_7B_3 = aabb$	
$(\lambda_0 \gamma_0 \sigma) = (37 \ 30 \ 80) \text{ cm}^{-1}; (S \ s_b \ \nu_b \ D^2) = (0.5 \ 1.3 \ 1.5 \ 18);$	
$N_{B-D} = [0000000 \ 00100];$	
$E = [61 \ 075 \ \mathbf{495} \ 220 \ 171 \ 187 \ \mathbf{622} \ \mathbf{518} \ 1117 \ 1132 \ 751 \ 861]; B_1(a)\uparrow, A_3(a)\uparrow, A_7(b)\downarrow$	
$E = [71 \ 064 \ \mathbf{535} \ 169 \ 105 \ 270 \ \mathbf{570} \ \mathbf{336} \ 850 \ 980 \ 847 \ 941]; B_1(a)\uparrow, A_3(a)\uparrow, A_6(a)\uparrow, A_7(b)\downarrow$	
$N_{B-D} = [0010000 \ 01100];$	
$E = [56 \ 74 \ 206 \ 162 \ 52 \ \mathbf{413} \ \mathbf{652} \ \mathbf{378} \ 1016 \ 1014 \ 687 \ 767]; B_1(a)\uparrow, A_6(a)\uparrow, A_7(b)\downarrow$	
$E = [87 \ 55 \ 205 \ 174 \ 84 \ \mathbf{398} \ \mathbf{706} \ \mathbf{465} \ 1052 \ 1001 \ 714 \ 864]; B_1(a)\uparrow, A_6(a)\uparrow,$	
$A_3A_6A_7B_3 = abba$	
$(\lambda_0 \gamma_0 \sigma) = (37 \ 30 \ 80) \text{ cm}^{-1}; (S \ s_b \ \nu_b \ D^2) = (0.5 \ 1.4 \ 1.5 \ 18);$	
$N_{B-D} = [0010000 \ 01100];$	
$E = [50 \ 18 \ \mathbf{375} \ 109 \ 29 \ 771 \ \mathbf{695} \ \mathbf{388} \ 1118 \ 137 \ 716 \ 1042]; B_1(a)\uparrow, A_3(a)\uparrow, A_7(b)\downarrow$	
$N_{B-D} = [0010100 \ 01100];$	
$E = [61 \ 24 \ \mathbf{307} \ 087 \ 35 \ \mathbf{632} \ \mathbf{581} \ \mathbf{383} \ 1089 \ 98 \ 644 \ 1006]; B_1(a)\uparrow, A_3(a)\uparrow, A_7(b)\downarrow, A_6(b)\downarrow$	
$N_{B-D} = [0010100 \ 01110];$	
$E = [41 \ 34 \ \mathbf{307} \ 067 \ 45 \ \mathbf{632} \ \mathbf{831} \ \mathbf{483} \ 889 \ 98 \ 694 \ 650]; B_1(a)\uparrow, A_3(a)\uparrow, A_6(b)\downarrow$	
$A_3A_6A_7B_3 = baba$	
$(\lambda_0 \gamma_0 \sigma) = (37 \ 30 \ 80) \text{ cm}^{-1}; (S \ s_b \ \nu_b \ D^2) = (0.5 \ 1.2 \ 1.3 \ 18);$	
$N_{B-D} = [0010100 \ 01100];$	
$E = [34 \ 27 \ 843 \ 23 \ 76 \ \mathbf{401} \ 1061 \ \mathbf{440} \ 710 \ \mathbf{293} \ 765 \ 773]; B_1(a)\uparrow, A_6(a)\uparrow, B_3(a)\uparrow,$	
$N_{B-D} = [0000000 \ 01100]; \text{ or } N_{B-D} = [0010000 \ 01100];$	
$E = [76 \ 87 \ 851 \ 233 \ 98 \ \mathbf{404} \ \mathbf{998} \ \mathbf{427} \ 836 \ 206 \ 742 \ 714]; B_1(a)\uparrow, A_6(a)\uparrow$	
$A_3A_6A_7B_3 = bbaa$	
$N_{B-D} = [0010100 \ 00110];$	
$(\lambda_0 \gamma_0 \sigma) = (37 \ 30 \ 80) \text{ cm}^{-1}; (S \ s_b \ \nu_b \ D^2) = (0.6 \ 1.0 \ 1.05 \ 14);$	
$E = [45 \ 39 \ \mathbf{680} \ 89 \ 101 \ 785 \ \mathbf{377} \ \mathbf{500} \ 855 \ 222 \ 815 \ 985]; B_1(a)\uparrow, A_7(a)\uparrow, A_3(b)\downarrow$	
$(\lambda_0 \gamma_0 \sigma) = (22 \ 30 \ 80) \text{ cm}^{-1}; (S \ s_b \ \nu_b \ D^2) = (0.54 \ 1.0 \ 1.2 \ 14);$	
$E = [20 \ 44 \ \mathbf{680} \ 217 \ 100 \ 810 \ 150 \ \mathbf{463} \ 940 \ \mathbf{316} \ 854 \ 1050]; B_1(a)\uparrow, B_3(a)\uparrow, A_3(b)\downarrow$	
$(\lambda_0 \gamma_0 \sigma) = (27 \ 30 \ 105) \text{ cm}^{-1}; (S \ s_b \ \nu_b \ D^2) = (0.5 \ 1.0 \ 1.2 \ 17);$	
$E = [61 \ 54 \ 795 \ 174 \ 56 \ \mathbf{630} \ 110 \ \mathbf{360} \ 820 \ \mathbf{350} \ 700 \ 910]; B_1(a)\uparrow, B_3(a)\downarrow, A_6(b)\downarrow$	
$(\lambda_0 \gamma_0 \sigma) = (22 \ 30 \ 80) \text{ cm}^{-1}; (S \ s_b \ \nu_b \ D^2) = (0.54 \ 1.0 \ 1.2 \ 14);$	
$E = [101 \ 54 \ 880 \ 237 \ 119 \ \mathbf{650} \ 168 \ \mathbf{423} \ \mathbf{650} \ \mathbf{356} \ 815 \ 920]; B_1(a)\uparrow, B_3(a)\uparrow, A_6(b)\downarrow, B_2(b)\downarrow$	

---

<sup>a</sup> Underlined values show the site energies of Chls *b*, underlined bold correspond to red-shifted Chls *b*, bold show blue-shifted Chls *a*. We also show assignments of the blue-shifted Chls *a* (marked by  $\uparrow$ ) and red-shifted Chls *b* (marked by  $\downarrow$ ). Notice that the site energies  $E$  do not include the reorganization energy shift due to strong coupling to phonons and vibrational modes (this shift is taken into account explicitly by introducing the  $\lambda$  matrices—see Appendixes C and D).

other words we need a pigment in that intermediate spectral region at this site to explain the kinetic data.

**TA Kinetics at 77 K.** Next we consider the fit of the 77 K kinetics using the *bbaa* model which gave the best fit of the data (the third *bbaa* model in Table 2 with blue-shifted  $B_3(a)$  and red-shifted  $A_6(b)$ ). Notice that a reasonable explanation of the spectra and kinetics can also be obtained with other models shown in Table 2.

The fit of the two-color TA kinetics measured for LHCII at 77 K upon 650 nm broad-band excitation is shown in Figures 3 and 4. The sequential pump–probe signal was calculated by solving the density matrix equation with the modified Redfield tensor instead of the traditional Redfield tensor. Notice that our previous modeling of the nonlinear kinetics in LHCII performed with the traditional Redfield tensor<sup>11</sup> revealed limitations of the standard Redfield theory. In particular, this theory underestimates the rates of interband  $b \rightarrow a$  transfer and overestimates the rates of slow intraband migration (see the Discussion in ref 11). Here we use the modified Redfield approach in order to obtain more realistic rates of energy transfer.

The 650  $\rightarrow$  647–650–659 nm kinetics show subpicosecond decay of the bleaching due to fast  $b \rightarrow a$  transfer. Shorter lifetimes at the blue side (compare the 647 and 650 nm decays) reflect intraband equilibration due to fast relaxation within a Chl *b* dimer. At the red side of the Chl *b* band (659 nm) the kinetics have a pronounced picosecond component due to the contribution of the long-lived red-shifted Chl *b* at site  $A_6$  and blue-shifted Chl *a* at  $B_3$  which are initially excited by a broad-band 20 nm pump pulse.

The 650  $\rightarrow$  665–668 nm kinetics show three clearly distinguishable components: (i) very fast decay near zero delay (the same as in the 650 nm kinetics but with a smaller amplitude) due to a contribution of the red wings of the *b* states with fast  $b \rightarrow a$  transfer, (ii) fast rising (resulting in nonmonotonic features near 200–300 fs) due to population of the *a* states via fast transfer from the *b* states, and (iii) slow picosecond decay of the long-lived “bottleneck” states ( $A_6(b)$  and  $B_3(a)$ ) in the 655–665 nm region.

The 650  $\rightarrow$  671–674 nm traces exhibit a subpicosecond rising time of the bleaching due to fast  $b \rightarrow a$  transfer followed by equilibration in the *a* band. The slow decay in the 671–674 nm region reflects the depopulation of long-lived states at the blue side of the *a* band ( $B_3(a)$  and  $A_7(a)$ ).

Finally, the 650  $\rightarrow$  677–683 nm kinetics show a formation of the bleaching band in the red wing of the Chl *a* region due to population of the lowest exciton states via direct (subpicosecond)  $b \rightarrow a$  transfer in combination with fast (subpicosecond) exciton relaxation within strongly coupled clusters in the *a* band. Slower components (subpicosecond to picosecond) reflect migration between spatially separated clusters in the *a* band and even more slow (several picoseconds) migration involving localized states in the *a* band.

**Population Dynamics (Exciton Representation).** Dynamics of the one-exciton populations upon 650 nm excitation are shown in Figure 5. The four higher exciton states  $k = 9$ –12 are determined by Chls *b*. These states show fast 200–300 fs decay due to  $b \rightarrow a$  transfer. The next three “bottleneck” states  $k = 6$ –8 are determined by contributions from blue-shifted Chl

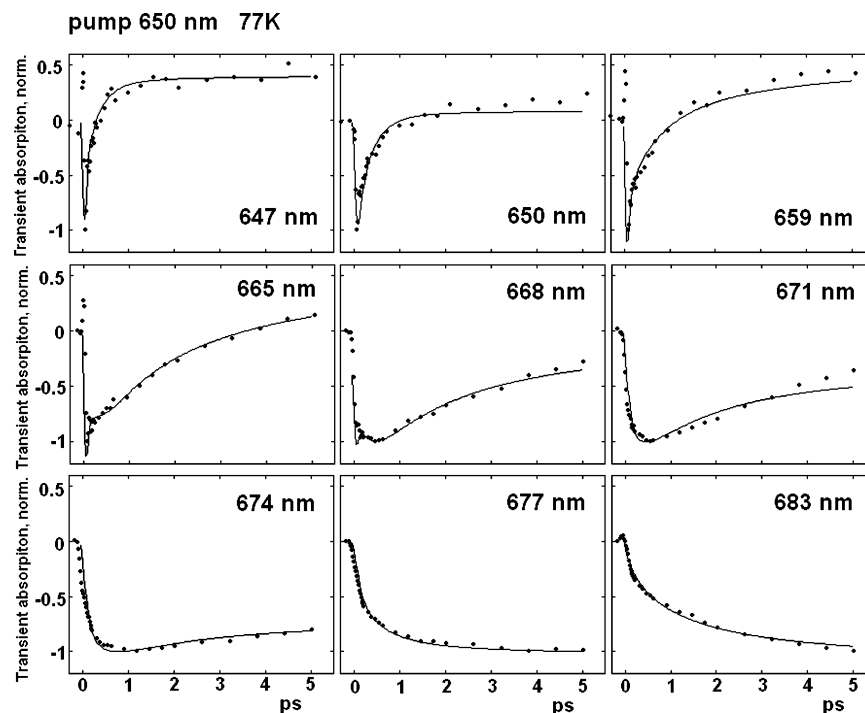


**Figure 3.** Two-color TA kinetics measured for LHCII at 77 K (points) and calculated with the modified Redfield theory (solid lines). The excitation wavelength is 650 nm, the pulse duration is 40 fs. Parameters of the model are listed in Table 2 (the third *bbaa* configuration with blue-shifted  $B_3(a)$  and red-shifted  $A_6(b)$ ). The sequential pump–probe signal was calculated by solving the density matrix equation with the modified Redfield tensor instead of the traditional Redfield tensor.

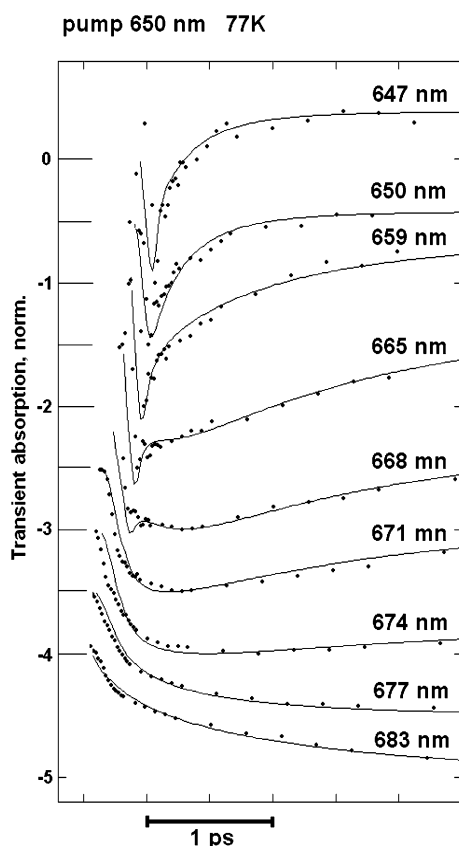


**Figure 4.** Comparison of the short-time part of the TA traces shown in Figure 3. To avoid an overlap of the curves we introduced a vertical shift of 0.5 and horizontal shift of 0.05 ps between neighboring traces. Horizontal lines show the zero level for each of eight curves.

*a* molecules at sites  $B_1$  and  $B_3$  and a red-shifted Chl *b* at  $A_6$ . They are characterized by fast decay due to the presence of  $B_1(a)$  and by slow decay (about 1 ps for  $k = 8$  and several

picoseconds for  $k = 6$  and 7) due to monomeric  $B_3(a)$  and  $A_6(b)$  pigments. The lowest states  $k = 1–5$  contain the exciton states of strongly coupled Chl *a* clusters as well as the monomeric Chl *a* pigment at  $A_7$ . The exciton states are characterized by very fast equilibration between them. We also observe slower dynamics between these states (see for example the slow rise in the  $k = 1$  population), corresponding to relaxation from higher monomeric states, migration between clusters, and equilibration between strongly coupled clusters and the monomeric  $A_7(a)$  state.

**Population Dynamics (Site Representation).** The equilibration dynamics (shown in the exciton basis in Figure 5) can be visualized in the site representation as shown in Figure 6. There are three groups of pigments: four Chls *b* with fast decay, three intermediate sites with slow decay, and five sites populated in the steady-state limit. The corresponding population dynamics are shown in Figure 6 in the case of short-wavelength excitation (the excitation conditions are the same as those in Figure 5).

Within the first group we observe a fast decay of the localized *b* states  $A_3(b)$  and  $B_2(b)$  due to strong coupling with the  $B_3(a)$  and  $A_2(a)$  sites, respectively. The very fast decay of the  $B_5(b)$  state is due to exciton relaxation within the  $B_5(b)–B_6(b)$  dimer.

The second group contains red-shifted  $A_6(b)$  and blue-shifted  $B_3(a)$  pigments absorbing in the 655–665 nm region. These pigments are initially populated by the pump pulse; subsequent energy transfer from the Chl *b* band further increases the  $B_3(a)$  population and also populates the long-lived monomeric (localized)  $A_7(a)$  state. At large delays the populations of the  $B_3(a)$  and  $A_7(a)$  monomeric states slowly decrease due to downhill transfers to the remaining Chls *a* states, i.e., to the exciton states of strongly coupled  $A_4(a)–A_5(a)$  and  $A_1(a)–A_2(a)–B_1(a)$  clusters. Thus, due to the presence of the three sites with slow decay, i.e.,  $B_3(a)$ ,  $A_6(b)$ , and  $A_7(a)$ , we have some bottleneck behavior in the site representation. These bottleneck sites are not exactly the same as the bottleneck states in the exciton representation, i.e., the  $k = 6–8$  levels. Only two of the long-



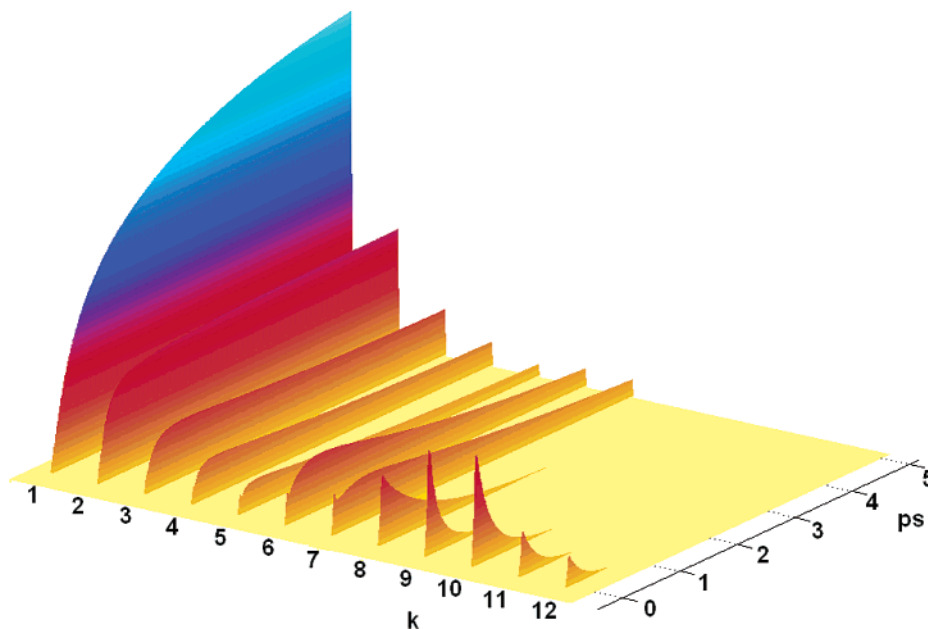


**Figure 5.** Dynamics of the one-exciton populations (averaged over disorder) at 77 K upon 650 nm excitation. The data were calculated with the same parameters as in Figures 3 and 4. Curves  $k = 9$ –12 show populations of the four  $b$  states,  $k = 6$ –8 lines show bottleneck states,  $k = 1$ –5 levels correspond to the five lowest  $a$  states.

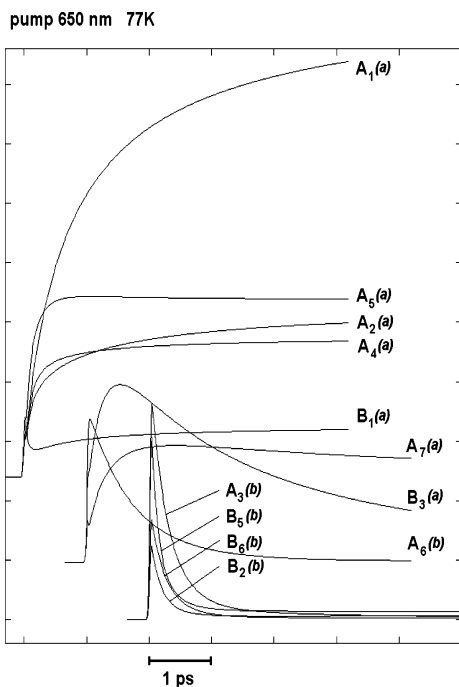


**Figure 6.** Dynamics of the site populations (averaged over disorder) at 77 K upon 650 nm excitation. The data were calculated with the same parameters as in Figures 3–5. Three groups of kinetics show populations of four  $b$  sites, monomeric bottleneck sites, i.e., red-shifted  $A_6(b)$ , blue-shifted  $B_3(a)$ , and  $A_7(a)$ , and five  $a$  sites, including strongly coupled  $A_4(a)$ – $A_5(a)$  and  $A_1(a)$ – $A_2(a)$ – $B_1(a)$  clusters.

lived sites, i.e.,  $B_3(a)$  and  $A_6(b)$ , participate in the  $k = 6$ –8 levels (the latter contain a mixture of long-lived sites  $B_3(a)$  and  $A_6(b)$  and one site  $B_1(a)$  with a fast decay). The third long-lived site  $A_7(a)$  does not contribute to the intermediate exciton states  $k = 6$ –8 at all (this site participates in the lower exciton states of the Chl  $a$  region).

The third group consists of the  $A_1(a)$ ,  $A_2(a)$ ,  $B_1(a)$ ,  $A_4(a)$ , and  $A_5(a)$  pigments. The blue-shifted  $B_1(a)$  is initially populated with subsequent very fast decay due to relaxation within the  $A_1(a)$ – $A_2(a)$ – $B_1(a)$  cluster. Equilibration within the  $A_4(a)$ –

$A_5(a)$  cluster as well as within the  $A_1(a)$ – $A_2(a)$ – $B_1(a)$  one is very fast (200–600 fs).<sup>11</sup> In Figure 6 one can observe slower transfer from the  $A_4(a)$ – $A_5(a)$  to the  $A_1(a)$ – $A_2(a)$ – $B_1(a)$  cluster. This transfer determines the slow increase of the  $A_1(a)$ ,  $A_2(a)$ , and  $B_1(a)$  populations. A redistribution of excitation energy between clusters is superimposed on slow picosecond transfer from the localized  $B_3(a)$  and  $A_7(a)$  states.

**TA Kinetics at 293 K: The Standard and Modified Redfield Theory.** The fit of the room-temperature kinetics is shown in Figures 7 and 8. To compare the two versions of the Redfield theory we used the density matrix picture with the standard Redfield tensor as well as the full-cumulant-expansion method with the relaxation kernel given by modified Redfield theory. We found that modified Redfield theory better reproduces specific features of the multicomponent kinetics, giving more correct amplitudes and time constants of the superimposed fast and slow components.

First, we note that the standard Redfield approach always underestimates the rates for the interband transfer, i.e., transfer between the states separated by a large energy gap (see the discussion in ref 36). Such a transfer is essentially determined by multiphonon processes not included in the traditional weak-coupled version of Redfield theory. The one-phonon character of the standard Redfield theory requires an increase of the spectral density in the high-frequency region to reproduce the experimentally observed interband rates. For example, in our previous paper we used a phenomenological spectral density with an intense high-frequency wing in order to reproduce the  $b \rightarrow a$  transfer in LHCII.<sup>11</sup> Interband transfer determines the fast subpicosecond (100–200 fs at room temperature) decay of the 653–671 nm kinetics (Figure 7). The standard Redfield calculation gives slower decay during 0–300 fs delays. On the other hand the modified Redfield theory allows a better explanation of the fast dynamics. In particular, it is possible to reproduce the 671 nm kinetics, where an initial fast (sub-100 fs) decay of the bleaching is superimposed on a slower (subpicosecond) rising component, producing a sharp peak around a 100 fs delay (a feature which is completely absent in the standard Redfield calculation).

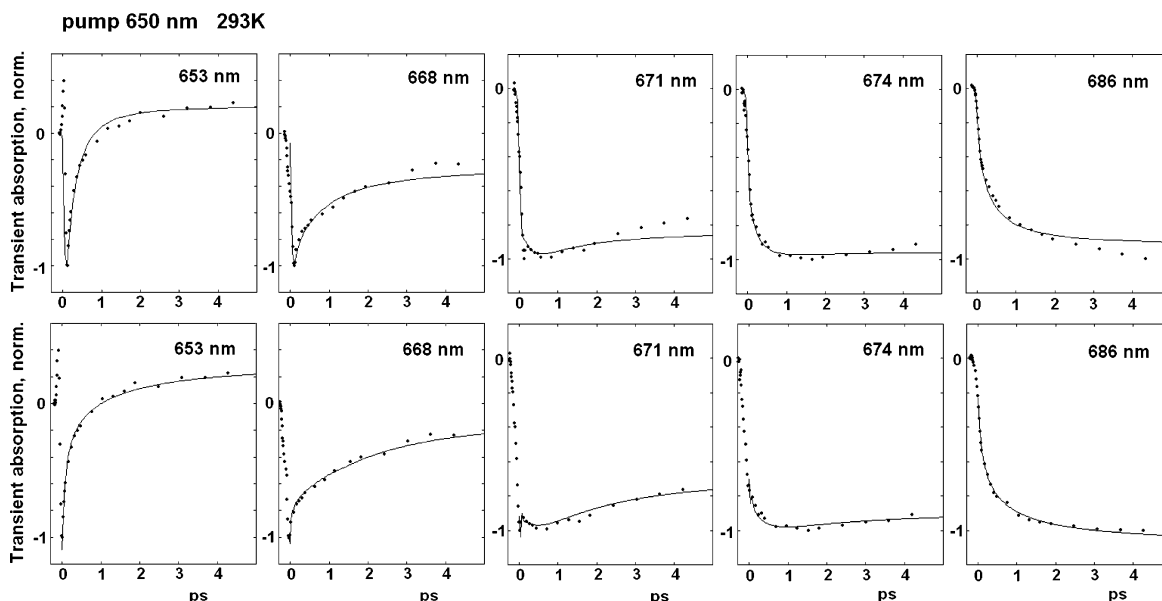


**Figure 7.** Modeling of the room-temperature TA kinetics measured for LHCII (points). The excitation wavelength is 650 nm, the pulse duration is 40 fs. Parameters of the model are the same as in Figure 3 (*bbaa* configuration). The top frames show the calculation using the density matrix equation with the standard Redfield relaxation tensor. In the bottom frames the calculation was done using the full-cumulant-expansion method with the modified Redfield tensor (we use the doorway–window representation of the pump–probe signal at positive delays).

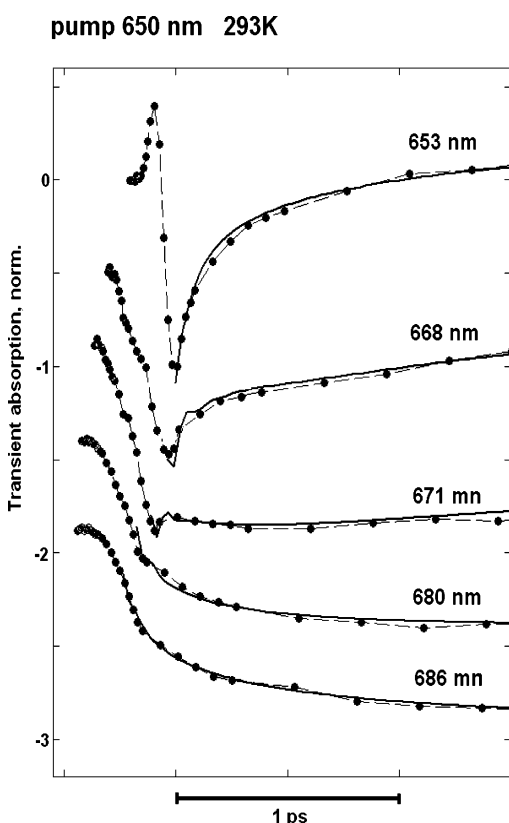


**Figure 8.** Comparison of a short-time part of the TA traces obtained with the modified Redfield theory as shown in Figure 7. To avoid an overlap of the curves we introduced some vertical and horizontal shifts of the curves.

Another feature which is difficult to reproduce is the slow picosecond component of intraband equilibration. The standard Redfield theory predicts too fast picosecond equilibration (Figure 7). Notice in this respect that in the standard theory the transfer rates are given by an overlap between the exciton wave functions (eqs B5), whereas the spectral overlap is given by the spectral density  $J(\omega)$ , which does not include the Stokes shift and the localization-induced broadening (eq D3) of the donor and accep-

tor states. In the standard Redfield picture the intraband transfers occur between strongly overlapping and narrow spectral forms. As a result the equilibration dynamics is always faster than the measured one. With the modified Redfield approach a more realistic line shape is included explicitly in the relaxation tensor, such that the transfer rates are distributed over a wider range depending on the degree of delocalization of the states involved. In particular, localized states are characterized by a broader phonon wing and a bigger Stokes shift. This can lead to a decrease in intraband transfer rates between monomeric states.

All together, we obtained too slow interband and too fast intraband transfer rates in the standard Redfield picture (when compared to the experimental data). On the other hand, both inter- and intraband rates were satisfactorily reproduced by the modified theory.

## Discussion and Conclusions

In this paper we report carefully measured energy-transfer dynamics in LHCII under annihilation-free conditions at various temperatures using Chl *b* (650 nm) excitation. To explain the results we have used a more realistic theory of exciton–phonon interactions in LHCII as compared with previous modeling.<sup>11</sup> In this model a diagonal exciton–phonon (exciton–vibrational) coupling is treated nonperturbatively.<sup>28</sup> This results in line shape asymmetry due to vibrational wings, a red shift of the zero-phonon transitions, and a Stokes shift of the steady-state fluorescence in proportion to the reorganization energy and the participation ratio. Similar approaches have recently been developed for linear exciton spectra.<sup>37,38</sup> However, in these papers the exciton relaxation (needed to model the nonlinear kinetics) was calculated in the weak coupling limit using the density matrix picture with the standard Redfield tensor. In the energy-transfer theory of Zhang et al.<sup>28</sup> an arbitrary strong diagonal phonon coupling was included in the relaxation tensor. Thus, multiphonon processes (neglected in the standard Redfield theory) are included in this modified version, leading to more realistic relaxation times.<sup>28,36</sup>

When modeling the linear spectra with this approach we found that a much better fit (as compared with the standard Redfield approach<sup>11</sup>) can be obtained in the intermediate region,

i.e., 655–665 nm. This allowed a better identification of the monomeric states in this region. We have obtained approximately the same exciton structure of the Chl *a* clusters as compared to our previous study, but in the present modeling the dipole strength is more uniformly distributed over the various states, i.e., there is no pronounced superradiance in any particular state as was suggested by some of our earlier models. However, the calculated thermally averaged superradiance is still in agreement with experiment.<sup>25</sup>

As in the previous modeling we found that a good quantitative fit of the linear spectra for any configuration does not guarantee that this model will explain the kinetics of nonlinear response. An adequate model should reproduce (i) the width and peak position of the bleaching near 650 nm (at zero delay) and near 678–680 nm (the steady-state bleaching of the Chl *a* band), (ii) multicomponent transfer kinetics between these regions, i.e., 650 → 680 nm kinetics, and (iii) kinetics in the 665–670 nm region including a contribution of the long-lived monomeric states to the whole 650 → 670 → 680 nm dynamics. We recall that in our previous study we found four configurations which gave a good quantitative explanation of features i and ii.<sup>11</sup> We were not able to check out feature iii due to lack of two-color pump–probe data at all wavelengths, but we supposed that only two of these four configurations will be consistent with the experimental kinetics. In this paper we revisited the problem performing detailed pump–probe studies and using more powerful theory which allows us to describe complicated energy-transfer dynamics with fast and slow, inter- and intraband kinetics superimposed. We found eight configurations after fitting features i and ii and four of them consistent with feature iii. These four configurations correspond to different assignment of the mixed states, i.e.,  $A_3A_6A_7B_3 = abba, baba, aabb, \text{ and } bbaa$ . It is remarkable that these configurations contain the *baba* and *bbaa* ones which were suggested previously.<sup>11</sup> We also found new configurations, i.e., *abba* and *aabb*. If we suppose that these four configurations occur in native antenna with equal probability, then the sites  $A_3$  and  $A_6$  each bind an average of 0.5 Chl *a* and 0.5 Chl *b*,  $A_7$  binds 0.5 Chl *a* and 1.5 Chl *b*, and  $B_3$  binds 1.5 Chl *a* and 0.5 Chl *b*. This means that they are really mixed states. For each of the four proposed configurations we adjusted independently the dipole moment orientations. These orientations turn out to be remarkably well-conserved. For the  $A_1, A_2, A_4, A_6, A_7, B_1, \text{ and } B_6$  sites the  $Q_y$  dipole moments are oriented along the  $N_A-N_C$  axis (direction “0”) and for  $B_3$  along the  $N_B-N_D$  axis (direction “1”). These orientations do not depend on pigment identities (at mixed sites  $A_6, A_7, \text{ and } B_3$ ). The  $A_3, A_5, B_2, \text{ and } B_5$  sites can have different orientations, i.e., “0” or “1”. Notice that these orientations are the same as in previous modeling. The only difference is that the “0” or “1” orientations are allowed for sites  $A_5$  and  $B_2$  (in our former model they always have the “0” orientation<sup>11</sup>).

While the general scheme of the whole energy-transfer process obtained in this study is basically the same as suggested previously,<sup>11</sup> we observed some nontrivial dynamics in the intermediate region between the Chl *b* and *a* bands. Here we have identified bottleneck states that are responsible for the slow components in the Chl *b* → *a* transfer. A systematic fit of the linear spectra and nonlinear kinetics enabled us to unravel the origin (and spectral signatures) of these long-lived “bottleneck” states, a feature that remained obscured in previous LHCII studies. In particular, we found that these “bottleneck” states are determined by two or three (depending on the model) monomeric Chls *a* or *b* shifted to the spectral region between the main absorption peaks of Chl *b* and Chl *a*. An interesting

conclusion is that these energy-shifted Chls are always (for all configurations) bound at mixed sites (i.e.  $A_3, A_6, A_7, \text{ or } B_3$ ).

**Acknowledgment.** V.N. was supported by the Russian-Dutch Research Cooperation Program (NWO, 047.009.014), a Visitor’s Grant from NWO (2004), and by the Russian Foundation for Basic Research, Grant No. 02-04-48779. The research was supported by the Foundation of Earth and Life Sciences (ALW), part of the Dutch Foundation of Scientific Research and the Human Frontiers in Science Program, Grant No. 1932802.

## Appendix A. Doorway–Window Representation of Pump–Probe

We use a doorway–window representation<sup>28,39</sup> for the sequential two-color pump–probe scheme. In order to compare standard and modified Redfield theories we neglect (i) the coherences between one-exciton states, (ii) population relaxation during the pump/probe pulse, and (iii) transfers of ground to one-exciton coherences and one- to two-exciton coherences. These restrictions are not essential for standard Redfield theory, but they are used in the modified version in its present form.<sup>28</sup> In the basis of one- and two-exciton eigenstates the transient absorption (TA) can be expressed as a sum of the photobleaching (PB), stimulated emission (SE), and excited-state absorption (ESA):

$$\begin{aligned} \text{PB} &= -\omega_2 W_{gg}(\omega_2) \sum_{k'} D_{k'k'}(0, \omega_1) \\ \text{SE} &= -\omega_2 \sum_k W_{kk}(\omega_2) D_{kk}(\tau, \omega_1) \\ \text{ESA} &= \omega_2 \sum_k \hat{W}_{kk}(\omega_2) D_{kk}(\tau, \omega_1) \end{aligned} \quad (\text{A1})$$

where  $\omega_1$  and  $\omega_2$  are pump and probe frequencies,  $\tau$  is the pump–probe delay, and  $g$  and  $k$  denote the ground and one-exciton states, respectively (an average over the static disorder is implied in eq A1). In the sequential pump–probe experiment the pump pulse creates a superposition of electronic states in the one-exciton manifold with the doorway amplitudes  $D_{kk}(0, \omega_1)$  together with the hole in the ground state given by  $-\sum_k D_{kk}(0, \omega_1)$ . The evolution of the excited-state wave packet due to exciton relaxation/migration during pump–probe delay is given by  $D_{kk}(\tau, \omega_1)$ . The ground-state hole is time-independent because one-exciton relaxation does not change the number of excitations, i.e.,  $-\sum_k D_{kk}(\tau, \omega_1) = \text{constant}$ . The absorption of a weak probe is determined by the overlap of the doorway and window wave packets (eq A1). The initial doorway amplitude  $D_{kk}(0, \omega_1)$ , and the window amplitudes  $W_{kk}(\omega_2)$ ,  $\hat{W}_{kk}(\omega_2)$ , and  $W_{gg}(\omega_2)$  are given by

$$\begin{aligned} D_{kk}(0, \omega_1) &= \int_{-\infty}^{\infty} dt' \int_0^{\infty} dt_1 \epsilon_1(t') \epsilon_1(t' - t_1) \times \\ &\quad d_{kg}^{e1} d_{kg}^{e1} D(\omega_{kg}, \omega_1, t_1) + \text{c.c.} \\ W_{kk}(\omega_2) &= \int_{-\infty}^{\infty} dt \int_0^{\infty} dt_3 \epsilon_2(t) \epsilon_2(t + t_3) \times \\ &\quad d_{kg}^{e2} d_{kg}^{e2} W(\omega_{kg}, \omega_2, t_3) + \text{c.c.} \\ \hat{W}_{kk}(\omega_2) &= \int_{-\infty}^{\infty} dt \int_0^{\infty} dt_3 \epsilon_2(t) \epsilon_2(t + t_3) \times \\ &\quad \sum_q d_{qk}^{e2} d_{qk}^{e2} \hat{W}(\omega_{qk}, \omega_2, t_3) + \text{c.c.} \\ W_{gg}(\omega_2) &= \int_{-\infty}^{\infty} dt \int_0^{\infty} dt_3 \epsilon_2(t) \epsilon_2(t + t_3) \times \\ &\quad \sum_k d_{kg}^{e2} d_{kg}^{e2} D(\omega_{kg}, \omega_2, t_3) + \text{c.c.} \end{aligned} \quad (\text{A2})$$

where  $\epsilon_1$  and  $\epsilon_2$  are the envelopes of the pump and probe pulses (they are taken to be real). Here we use indices  $g, k$ , and  $q$  for ground, one- and two-exciton states, respectively. Transition dipoles  $d_{kg}$  and  $d_{qk}$  correspond to  $g \rightarrow k$  and  $k \rightarrow q$  transitions with the transition frequencies  $\omega_{kg}$  and  $\omega_{qk}$ , respectively. Transition frequencies  $\omega_{ab} = \omega_a - \omega_b$  are given by the difference of frequencies of the  $a$  and  $b$  eigenstates. Superscripts  $e1/e2$  denote projection of the transition dipoles to the polarization vectors of the pump/probe pulses.  $D, W$ , and  $\hat{W}$  are the line shape functions describing a dephasing during the electronic coherence periods  $t_1$  and  $t_3$ . They correspond to ground-state absorption, excited-state emission, and excited-state absorption, respectively. Note that the window amplitude  $W_{gg}(\omega_2)$  depends on the  $D$  function, being determined by the ground-state absorption. Integration over  $t$  and  $t'$  can be done analytically if one specifies the pulse shape. For example, supposing Gaussian pulses  $\epsilon_{1,2}(t) = \pi^{-1/4} \tau_{1,2}^{-1/2} \exp(-t^2/2\tau_{1,2}^2)$  with fwhm of  $1.66\tau_{1,2}$  we get

$$\begin{aligned} D_{kk}(0, \omega_1) &= d_{kg}^{e1} d_{kg}^{e1} \int_0^\infty dt_1 e^{-(t_1/2\tau_1)^2} \times \\ &\quad D(\omega_{kg}, \omega_1, t_1) + \text{c.c.} \\ W_{kk}(\omega_2) &= d_{kg}^{e2} d_{kg}^{e2} \int_0^\infty dt_3 e^{-(t_3/2\tau_2)^2} \times \\ &\quad W(\omega_{kg}, \omega_2, t_3) + \text{c.c.} \\ \hat{W}_{kk}(\omega_2) &= \sum_q d_{qk}^{e2} d_{qk}^{e2} \int_0^\infty dt_3 e^{-(t_3/2\tau_2)^2} \times \\ &\quad \hat{W}(\omega_{qk}, \omega_2, t_3) + \text{c.c.} \\ W_{gg}(\omega_2) &= \sum_k d_{kg}^{e2} d_{kg}^{e2} \int_0^\infty dt_3 e^{-(t_3/2\tau_2)^2} \times \\ &\quad D(\omega_{kg}, \omega_2, t_3) + \text{c.c.} \end{aligned} \quad (\text{A3})$$

In modified Redfield theory the line shape functions are

$$\begin{aligned} D(\omega_{kg}, \omega_1, t_1) &= \exp\{-i(\omega_{kg} - \omega_1)t_1 - g_{kkkk}(t_1)\} \\ W(\omega_{kg}, \omega_2, t_3) &= \exp\{-i(\omega_{kg} - \omega_2)t_3 + 2i\lambda_{kkkk}^* t_3 - g_{kkkk}^*(t_3)\} \\ \hat{W}(\omega_{qk}, \omega_2, t_3) &= \exp\{-i(\omega_{qk} - \omega_2)t_3 - g_{kkkk}(t_3) - g_{qqqq}(t_3) + \\ &\quad 2g_{kkqq}(t_3) + 2i(\lambda_{kkqq} - \lambda_{kkkk})t_3\} \end{aligned} \quad (\text{A4})$$

The line-broadening  $g$  functions and reorganization energy values  $\lambda$  (given by eq C2 for our model and calculated by Meier et al.<sup>40</sup> in the general case) in these expressions appear due to strong diagonal exciton-phonon coupling. Transition frequencies in eq A4 correspond to the first moment of the absorption lines. They are determined by the eigenvalues of the exciton Hamiltonian, i.e.,  $\omega_k$  and  $\omega_q$ , which do not include a reorganization energy shift. In the presence of strong phonon coupling the thus-determined transition frequencies are different from the frequencies of the zero-phonon transitions.

In the weak coupling limit (traditional Redfield theory) eqs A2 can be obtained from the density matrix equation (expanded up to the third order with respect to the external fields) under assumptions i–iii. The corresponding line shape functions in this case are

$$\begin{aligned} D(\omega_{kg}, \omega_1, t_1) &= \exp\{-i(\omega_{kg} - \omega_1)t_1 - R_{kgkg} t_1\} \\ W(\omega_{kg}, \omega_2, t_3) &= \exp\{-i(\omega_{kg} - \omega_2)t_3 - R_{kgkg} t_3\} \\ \hat{W}(\omega_{qk}, \omega_2, t_3) &= \exp\{-i(\omega_{qk} - \omega_2)t_3 - R_{qkqk} t_3\} \end{aligned} \quad (\text{A5})$$

where dephasing of the ground to one-exciton coherences and

one- to two-exciton coherences is given by the corresponding elements of the standard Redfield tensor. Exponential decay determines the Lorentzian line shapes in the standard Redfield approach.

For both theories the time evolution of the initially created doorway packet is given by

$$\frac{d}{d\tau} D_{kk}(\tau, \omega_1) = -\sum_{k,k'} R_{kk'k'} D_{k'k}(\tau, \omega_1) \quad (\text{A6})$$

with the initial conditions given by the first of eqs A2 and the relaxation tensor calculated according to the standard or modified Redfield approach.

## Appendix B. Standard Redfield Tensor

Here we calculate the Redfield tensor in a basis of eigenstates labeled by indices  $a, b, c, d$  (which can take values  $g, k$ , or  $q$ , i.e., we calculate the full two-exciton Redfield tensor). In the limit of weak system-bath coupling the dynamics within one- and two-exciton manifolds is given by the Redfield relaxation tensor which can be written in a form<sup>41,42</sup>

$$\begin{aligned} R_{a'b'ab} &= -Y_{aa'bb'} - Y_{bb'aa'}^* + \delta_{bb'} \sum_c Y_{acca'} + \\ &\quad \delta_{aa'} \sum_c Y_{bccb'}^* \\ Y_{abcd} &= \int_0^\infty dt \int_{-\infty}^\infty \frac{d\omega}{4\pi} C_{abcd}(\omega) e^{i\omega_{ab}t} \times \\ &\quad \left[ \coth \frac{\omega}{2k_B T} \cos \omega t - i \sin \omega t \right] \\ C_{abcd}(\omega) &= \frac{i}{2} \int_{-\infty}^\infty dt e^{i\omega t} \langle [f_{ab}(t) f_{cd}(0)] \rangle \\ H_{\text{ex-ph}} &= \sum_{a,b} f_{ab} |a\rangle \langle b| \end{aligned} \quad (\text{B1})$$

where  $H_{\text{ex-ph}}$  is the exciton-phonon Hamiltonian,  $f_{ab}$  denotes bath-induced fluctuations in the exciton eigenstate basis,  $\omega_{ab} = \omega_a - \omega_b$  is the difference of frequencies of the  $a$  and  $b$  eigenstates,  $C_{abcd}(\omega)$  is the matrix of spectral densities in the eigenstate representation, and  $k_B T$  is the temperature measured in the same units as  $\omega$ . The matrix of spectral densities is connected with the line-broadening function

$$\begin{aligned} g_{abcd}(t) &= -\int_{-\infty}^\infty \frac{d\omega}{2\pi\omega^2} C_{abcd}(\omega) \times \\ &\quad \left[ \coth \frac{\omega}{2k_B T} (\cos \omega t - 1) - i(\sin \omega t - \omega t) \right] \end{aligned} \quad (\text{B2})$$

that determines linear (first-order) and nonlinear (third-order) optical responses.<sup>28,40</sup> Thus, the spectral density  $C_{abcd}(\omega)$  can be extracted from spectroscopic data.

To calculate the Redfield tensor explicitly we first specify the exciton-phonon Hamiltonian in the site representation

$$\begin{aligned} H_{\text{ex-ph}} &= \sum_{n,m} f_{nm} |n\rangle \langle m| + \sum_{m>n, m'>n'} f_{nmn'm'} |nm\rangle \langle n'm'| + \\ &\quad \sum_{n,n'} f_{nnn'n'} |nn\rangle \langle n'n'| \end{aligned} \quad (\text{B3})$$

where the first and second sums account for a bath-induced relaxation in the one- and two-exciton manifolds of an aggregate made of two-level molecules. The third term appears in the case



of three-level molecules and reflects a contribution of doubly excited states. We neglected the terms such as  $|g\rangle\langle n|$ ,  $|g\rangle\langle nm|$ , and  $|n\rangle\langle nm|$  responsible for radiationless decay of one- and two-exciton states, and  $|n\rangle\langle nm|$  responsible for singlet–singlet annihilation. We further suppose diagonal disorder, i.e.,  $f_{nm} = \delta_{nm}f_n$ ,  $f_{nm'm'} = \delta_{nm'}\delta_{mm'}(f_n + f_m)$ , and  $f_{nm'n'} = \delta_{nm'}f_{nn'}$  without intersite correlations, i.e.,  $\langle f_n f_{n'} \rangle = \delta_{nn'}v_n$  and  $\langle f_{nn'} f_{n'n'} \rangle = \delta_{nn'}w_n$ . This model implies that each molecule has its own independent bath. We also neglect correlation between singly and doubly excited states of one molecule  $\langle f_{nn'} f_n \rangle$ , which means that  $S_1$  and  $S_2$  also have independent coupling to the bath. This is a stronger assumption, because the dynamic disorder of different electronic states within one molecule is more correlated than the disorder acting on different molecules. Notice, however, that generalization to the case of more complicated disorder is straightforward: it will lead to additional terms in the Redfield tensor that we reject here for simplicity.

For this model the spectral density in the site representation is  $C_{nm'm'}(\omega) = \delta_{nm}\delta_{nn'}\delta_{mm'}v_n C(\omega)$  or  $w_n C(\omega)$  for double-excited states, where  $v_n$  (or  $w_n$ ) is a dimensionless factor. A transformation to the eigenstate representation is given by

$$|k\rangle = \sum_n c_n^k |n\rangle; \quad |q\rangle = \sum_{m \geq n} c_{nm}^q |nm\rangle \quad (\text{B4})$$

Using eqs B1–B4 we obtain the full Redfield tensor as

$$\begin{aligned} R_{kgk'g} &= \sum_{s,n} c_n^k c_n^{k'} (c_n^s)^2 v_n J_{sk'} \\ R_{qgq'g} &= \sum_{r,n} c_{nn}^q c_{nn}^r c_{nn}^{q'} w_n J_{rq'} + \\ &\quad \sum_{r,m > n, m' > n'} c_{nm}^q c_{nm}^r c_{n'm'}^{q'} J_{rq'} \times \\ &\quad (\delta_{nn'}v_n + \delta_{nm'}v_n + \delta_{mm'}v_m + \delta_{mm'}v_m) \\ R_{kk'pp'} &= \delta_{k'p'} R_{kpgp} + \delta_{kp} R_{k'gp'g} - \\ &\quad \sum_n c_n^k c_n^{k'} c_n^p c_n^{p'} v_n (J_{kp} + J_{k'p'}) \\ R_{qq'q'k} &= \delta_{kk'} R_{qgq'g} + \delta_{qq'} R_{k'gp'g} - \\ &\quad \sum_{m > n} c_{nm}^q c_{nm}^{q'} (c_n^k c_n^{k'} v_n + c_m^k c_m^{k'} v_m) (J_{kk'}^* + J_{qq'}) \end{aligned} \quad (\text{B5})$$

where  $k$  and  $p$  stand for one-exciton states and  $q$  and  $r$  denote two-exciton states. The effective spectral density is

$$J_{ab} = \int_0^\infty dt e^{-i\omega_{ab}t} \int_{-\infty}^\infty \frac{d\omega}{4\pi} C(\omega) \left[ \coth \frac{\omega}{2k_B T} \cos \omega t - i \sin \omega t \right] \quad (\text{B6})$$

where  $C(\omega)$  is the site-independent spectral density profile (in the site representation). A possible site-to-site variation of coupling strength is given by factors  $v_n$  and  $w_n$  in eq B5.

The  $C(\omega)$  profile can be extracted from spectroscopic data. The simplest way is to determine it from the low-temperature fluorescence, where only one exciton level (i.e., the lowest level with nonbroadened zero-phonon origin and vibronic satellites) contributes to the emission. The inhomogeneous broadening can be excluded using the fluorescence line-narrowing technique. Note that in the case of a harmonic bath (discrete oscillators, continuous distribution of oscillators, Brownian oscillator model)  $C(\omega)$  is temperature-independent. Because it is determined from the low-temperature fluorescence data, this spectral density can

be used for modeling of various spectral responses at different temperatures.

We note that there are three spectral densities: The first is the spectral density in the eigenstate representation  $C_{abcd}(\omega)$  which determines the spectral line shapes for linear and nonlinear responses. The second is the spectral density in the site representation  $C_{nm'm'}(\omega)$ . In the model of uncorrelated diagonal disorder this one is characterized by a site-independent profile  $C(\omega)$  connected with the eigenstate representation  $C_{abcd}(\omega)$  by a factor equal to the fourth power of the wave function amplitude (see eqs B5). Thus, the coupling strength acting on eigenstates is less than that acting on individual sites by a factor roughly equal to the delocalization degree of the corresponding eigenstates. The third is the temperature-dependent function  $J_{ab}(\omega_{ab})$  which determines the relaxation rates between the eigenstates. It is important that the spectral line shapes expressed through the line-broadening function  $g(t)$  contain  $C(\omega)/\omega^2$ . Thus, the  $J(\omega)$  profile is significantly different from the experimental profiles. The latter typically have a relatively weak phonon (vibrational) wing, whereas the  $C(\omega)$  and  $J(\omega)$  profiles show strong increase to higher frequencies. As an example, Figure 1 shows the  $J(\omega)$  function determined from the low-temperature fluorescence of LHCII.

### Appendix C. Modified Redfield Tensor

The modified Redfield tensor corresponding to the one-exciton population transfers is given by<sup>28</sup>

$$\begin{aligned} R_{kk'k'k} &= -2\text{Re} \int_0^\infty dt \hat{W}(\omega_{kk'}, 0, t) \{ \ddot{g}_{kk'k'k}(t) - \{ \dot{g}_{k'kk'k}(t) - \\ &\quad \dot{g}_{k'kkk}(t) + 2i\lambda_{k'kk'k}(t) \} \times \{ \dot{g}_{k'k'kk}(t) - \dot{g}_{kkkk}(t) + 2i\lambda_{k'k'kk}(t) \} \} \end{aligned} \quad (\text{C1})$$

In the model of uncorrelated diagonal disorder the  $\mathbf{g}$  matrices are connected with the  $\mathbf{g}$  function

$$\begin{aligned} g_{kk'k'k'''}(t) &= \sum_n c_n^k c_n^{k'} c_n^{k''} c_n^{k'''} v_n g(t) \\ g_{kkqq}(t) &= \sum_{n < m} (c_{nm}^q c_n^{k'})^2 (\delta_{nn'}v_n + \delta_{mm'}v_m) g(t) \\ g_{qqqq}(t) &= \sum_{\substack{n < m \\ n' < m'}} (c_{nm}^q c_{n'm'}^q)^2 (\delta_{nn'}v_n + \delta_{mm'}v_m + \delta_{mm'}v_m + \\ &\quad \delta_{mm'}v_m) g(t) + \sum_n (c_{nn}^q)^4 w_n g(t) \end{aligned} \quad (\text{C2})$$

and the same equations connect the  $\lambda$  matrices with the  $\lambda$  value, where

$$\begin{aligned} g(t) &= - \int_{-\infty}^\infty \frac{d\omega}{2\pi\omega^2} C(\omega) \times \\ &\quad \left[ \coth \frac{\omega}{2k_B T} (\cos \omega t - 1) - i(\sin \omega t - \omega t) \right] \\ \lambda &= - \lim_{t \rightarrow \infty} \frac{d}{dt} \text{Im} \{ g(t) \} = \int_{-\infty}^\infty \frac{d\omega}{2\pi\omega} C(\omega) \end{aligned} \quad (\text{C3})$$

### Appendix D. Linear Spectra

The absorption (OD), linear dichroism (LD), and steady-state nonselective fluorescence (FL) spectra are given by

$$\text{FL}(\omega) = \omega \sum_k P_k d_{kg}^2 \text{Re} \int_0^\infty dt e^{i(\omega - \omega_{kg})t + i\lambda_{kkkk}t - g_{kkkk}^*(t) - R_{kkkk}t}$$

$$\begin{aligned}
 \text{OD}(\omega) &= \omega \sum_k d_{kg}^2 \text{Re} \int_0^\infty dt e^{i(\omega - \omega_{kg})t - i\lambda_{kkkk}t - g_{kkkk}(t) - R_{kkkk}t}, \\
 R_{kkkk} &= - \sum_{k' \neq k} R_{k'k'kk} \\
 \text{LD}(\omega) &= \omega \sum_k \left( -d_{kgz}^2 + \frac{1}{2}d_{kgx}^2 + \frac{1}{2}d_{kgy}^2 \right) \times \\
 &\quad \text{Re} \int_0^\infty dt e^{i(\omega - \omega_{kg})t - i\lambda_{kkkk}t - g_{kkkk}(t) - R_{kkkk}t} \quad (\text{D1})
 \end{aligned}$$

where  $P_k$  denotes the steady-state population of the  $k$ th state,  $d_{kgz}$  denotes projection to the  $z$ -axis which is normal to the membrane planes, and  $d_{kgx}$  and  $d_{kgy}$  are the in-plane components. We have introduced into eqs D1 a relaxation-induced broadening of the exciton states given by their inverse lifetimes, i.e.,  $R_{kkkk}$  as suggested in refs 38 and 46 (this relaxation term was not included in the original theory of Zhang et al.<sup>28</sup>). Equations D1 give homogeneous line shapes. In the presence of static disorder (for example site inhomogeneity) the homogeneous OD, LD, and FL profiles should be averaged over a random distribution of the site energies that will perturb energies and eigenfunctions of the exciton states. To construct the spectral density profile we use the sum of an overdamped Brownian oscillator and resonance contributions due to high-frequency modes

$$\begin{aligned}
 C(\omega) &= 2\lambda_0 \frac{\omega\gamma_0}{\omega^2 + \gamma_0^2} + \sum_{j=1,2,\dots} 2\lambda_j \omega_j^2 \times \\
 &\quad \frac{\omega\gamma_j}{(\omega_j^2 - \omega^2)^2 + \omega^2\gamma_j^2}, \quad \lambda_j = S_j\omega_j \\
 \lambda &= \int_{-\infty}^{\infty} \frac{d\omega}{2\pi\omega} C(\omega) = \lambda_0 + \sum_{j=1,2,\dots} \lambda_j \quad (\text{D2})
 \end{aligned}$$

where  $2\lambda$  is the Stokes shift and  $S_j$  is the Huang–Rhys factor of the  $j$ th vibrational mode. Parameters of vibrational modes can be taken from the low-temperature FL line-narrowing data (or from molecular dynamics simulation) and then adjusted from the fit of the linear spectra at different temperatures using eqs D1, C2, C3. The thus-determined  $g$  function can then be used for simulation of nonlinear responses (see Appendixes A, B, and C). Notice that according to eq C2

$$\begin{aligned}
 g_{kkkk}(t) &= \sum_n (c_n^k)^4 v_n g(t) \\
 \lambda_{kkkk} &= \sum_n (c_n^k)^4 v_n \lambda \quad (\text{D3})
 \end{aligned}$$

i.e., line-broadening functions and reorganization energies in the exciton representation ( $g_{kkkk}$  and  $\lambda_{kkkk}$ ) are smaller than in the site representation ( $g$  and  $\lambda$  in the case  $v_n \approx 1$ ) by a factor of  $1/\sum (c_n^k)^4$ . The latter is known as the inverse participation ratio which is equal to a delocalization length of the individual exciton states.<sup>43–45</sup>

## References and Notes

- (1) van Amerongen, H.; van Grondelle, R. *J. Phys. Chem. B* **2001**, *105*, 604.
- (2) Kühlbrandt, W.; Wang, D. N.; Fujiyoshi, Y. *Nature* **1994**, *367*, 614.
- (3) Remelli, R.; Varotto, C.; Sandona, D.; Croce, R.; Bassi, R. *J. Biol. Chem.* **1999**, *274*, 33510.
- (4) Rogl, H.; Kühlbrandt, W. *Biochemistry* **1999**, *38*, 16214.
- (5) Yang, C.; Kosemund, K.; Cornet, C.; Paulsen, H. *Biochemistry* **1999**, *38*, 16205.
- (6) Rogl, H.; Schödel, R.; Lokstein, H.; Kühlbrandt, W.; Schubert, A. *Biochemistry* **2002**, *41*, 2281.
- (7) Bassi, R.; Croce, R.; Cugini, D.; Sandona, D. *Proc. Natl. Acad. Sci. U.S.A.* **1999**, *96*, 10056.
- (8) Simonetto, R.; Crimi, M.; Sandona, D.; Croce, R.; Cinque, G.; Breton, J.; Bassi, R. *Biochemistry* **1999**, *38*, 12974.
- (9) İşeri, E. I.; Gülen, D. *Eur. Biophys. J.* **2001**, *30*, 344.
- (10) Gülen, D.; van Grondelle, R.; van Amerongen, H. *J. Phys. Chem. B* **1997**, *101*, 7256.
- (11) Novoderezhkin, V.; Salverda, J. M.; van Amerongen, H.; van Grondelle, R. *J. Phys. Chem. B* **2003**, *107*, 1893.
- (12) Renger, Th.; May, V. *Phys. Rev. Lett.* **2000**, *84*, 5228.
- (13) Bittner, T.; Wiederrecht, G. P.; Irrgang, K.-D.; Renger, G.; Wasielewski, M. R. *Chem. Phys.* **1995**, *194*, 311.
- (14) Visser, H. M.; Kleima, F. J.; van Stokkum, I. H. M.; van Grondelle, R.; van Amerongen, H. *J. Chem. Phys.* **1996**, *210*, 297.
- (15) Kleima, F. J.; Gradinaru, C. C.; Calkoen, F.; van Stokkum, I. H. M.; van Grondelle, R.; van Amerongen, H. *Biochemistry* **1997**, *36*, 15262.
- (16) Gradinaru, C. C.; Özdemir, S.; Gülen, D.; van Stokkum, I. H. M.; van Grondelle, R.; van Amerongen, H. *Biophys. J.* **1998**, *75*, 3064.
- (17) Gradinaru, C. C.; van Stokkum, I. H. M.; Pascal, A. A.; van Grondelle, R.; van Amerongen, H. *J. Phys. Chem. B* **2000**, *104*, 9330.
- (18) Du, M.; Xie, X.; Mets, L.; Fleming, G. R. *J. Phys. Chem.* **1994**, *98*, 4736.
- (19) Bittner, T.; Irrgang, K.-D.; Renger, G.; Wasielewski, M. R. *J. Phys. Chem.* **1994**, *98*, 11821.
- (20) Connelly, J. P.; Müller, M. G.; Hücke, M.; Gatzert, G.; Mullineaux, C. W.; Ruban, A. V.; Horton, P.; Holzwarth, A. R. *J. Phys. Chem. B* **1997**, *101*, 1902.
- (21) Agarwal, R.; Krueger, B. P.; Scholes, G. D.; Yang, M.; Yom, J.; Mets, L.; Fleming, G. R. *J. Phys. Chem. B* **2000**, *104*, 2908.
- (22) Salverda, J. M.; Vengris, M.; Krueger, B. P.; Scholes, G. D.; Czarnoleski, A. R.; Novoderezhkin, V.; van Amerongen, H.; van Grondelle, R. *Biophys. J.* **2003**, *84*, 450.
- (23) Yang, M.; Fleming, G. R. *J. Chem. Phys.* **1999**, *111*, 27.
- (24) Schubert, A.; Beenken, W. J. D.; Stiel, H.; Voigt, B.; Leupold, D.; Lokstein, H. *Biophys. J.* **2002**, *82*, 1030.
- (25) Palacios, M. A.; de Weerd, F. L.; Ihalainen, J. A.; van Grondelle, R.; van Amerongen, H. *J. Phys. Chem. B* **2002**, *106*, 5782.
- (26) Redfield, A. G. *Adv. Magn. Reson.* **1965**, *1*, 1.
- (27) Pollard, W. T.; Felts, A. K.; Friesner, R. A. *Adv. Chem. Phys.* **1996**, *93*, 77.
- (28) Zhang, W. M.; Meier, T.; Chernyak, V.; Mukamel, S. *J. Chem. Phys.* **1998**, *108*, 7763.
- (29) Peterman, E. J. G.; Pullerits, T.; van Grondelle, R.; van Amerongen, H. *J. Phys. Chem. B* **1997**, *101*, 4448.
- (30) Peterman, E. J. G.; Dukker, F. M.; van Grondelle, R.; van Amerongen, H. *Biophys. J.* **1995**, *69*, 2670.
- (31) van Amerongen, H.; Kwa, S. L. S.; van Bolhuis, B. M.; van Grondelle, R. *Biophys. J.* **1994**, *67*, 837.
- (32) Kühn, O.; Sundström, V. *J. Chem. Phys.* **1997**, *107*, 4154.
- (33) Novoderezhkin, V.; van Grondelle, R. *J. Phys. Chem. B* **2002**, *106*, 6025.
- (34) Pieper, J.; Voigt, J.; Small, G. J. *J. Phys. Chem. B* **1999**, *103*, 2319.
- (35) Knox, R. S.; Spring, B. Q. *Photochem. Photobiol.* **2003**, *77* (5), 497.
- (36) Yang, M.; Fleming, G. R. *Chem. Phys.* **2002**, *275*, 355.
- (37) Schütze, J.; Brüggemann, B.; Renger, Th.; May, V. *Chem. Phys.* **2002**, *275*, 333.
- (38) Renger, Th.; Marcus, R. A. *J. Chem. Phys.* **2002**, *116*, 9997.
- (39) Mukamel, S. *Principles of Nonlinear Optical Spectroscopy*; Oxford University Press: New York, 1995.
- (40) Meier, T.; Chernyak, V.; Mukamel, S. *J. Chem. Phys.* **1997**, *107*, 8759.
- (41) Chernyak, V.; Minami, T.; Mukamel, S. *J. Chem. Phys.* **2000**, *112*, 7953.
- (42) Dahlbom, M.; Minami, T.; Chernyak, V.; Pullerits, T.; Sundström, V.; Mukamel, S. *J. Phys. Chem. B* **2000**, *104*, 3976.
- (43) Fidler, H.; Knoester, J.; Wiersma, D. A. *J. Chem. Phys.* **1991**, *95*, 7880.
- (44) Meier, T.; Chernyak, V.; Mukamel, S. *J. Phys. Chem. B* **1997**, *101*, 7332.
- (45) Novoderezhkin, V.; Monshouwer, R.; van Grondelle, R. *Biophys. J.* **1999**, *77*, 666.
- (46) Ohta, K.; Yang, M.; Fleming, G. R. *J. Chem. Phys.* **2001**, *115*, 7609.